

Numerical Simulations of Waves over Large Crater Topography in the Atmosphere

NANCY SOONTIENS, MAREK STASTNA, AND MICHAEL L. WAITE

Department of Applied Mathematics, University of Waterloo, Waterloo, Ontario, Canada

(Manuscript received 6 August 2012, in final form 24 October 2012)

ABSTRACT

Numerical simulations are used to investigate waves generated by flow over crater topography of diameter 100 km in an idealized atmosphere. The atmosphere is stratified with a constant buoyancy frequency profile and the background wind is constant. This study describes the development of a low-level jet along the upstream crater slope and its interaction with the cooler air within the crater valley. This interaction results in a hydraulic jump–like structure that acts as a modified topography, forcing a beam of secondary waves. The hydraulic jump is formed by a retreating gravity current as the cool air within the crater readjusts after the initial tilting of potential temperature contours. A two-dimensional simulation is used to compare features such as wave overturning in two and three dimensions. Several variations on the atmosphere's profile are considered, including an atmosphere with reduced constant stratification and an atmosphere that is unstratified within the crater. These results indicate that the stratification within the crater is an important component in the development of the hydraulic jump. Also, several topographic modifications are included, such as a crater with no rims and a crater with reduced diameter. These comparisons reveal that the crater rims have little impact on the general wave pattern and that the crater curvature can influence wave breaking and lateral deflections. In addition, cases with rotation break the symmetry and induce more overturning in one-half of the crater.

1. Introduction

Internal gravity waves generated by flow over topography play a key role in the dynamics of the atmosphere. These waves, often called mountain waves or lee waves, have been examined in many frameworks, including analytical mathematical models (e.g., Long 1953; Smith 1980), numerical simulations (e.g., Klemp and Lilly 1978; Afanasyev and Peltier 1998), laboratory experiments (e.g., Baines and Smith 1993; Gyüre and Jánosi 2003), and atmospheric observations (e.g., Holmboe and Klieforth 1957; Caccia et al. 1997). A thorough overview of the literature is provided in reviews such as Smith (1989a), Baines (1995), and Wurtele et al. (1996). The degree of complexity in these studies has increased over the years, and they now include three-dimensional, nonhydrostatic, and nonlinear effects, as well as complicated topographic and atmospheric profiles. This study investigates flow over three-dimensional crater

topography and the generation of internal waves in an idealized atmosphere.

Early studies on mountain waves and flow over topography focused on the two-dimensional problem, but more recently there has been increased interest in three-dimensional effects (e.g., Andreassen et al. 1994; Afanasyev and Peltier 1998). There are significant differences between two- and three-dimensional mountain waves. Smith (1980) used linear theory to study three-dimensional hydrostatic flow over an isolated mountain and observed that wave energy is present at large horizontal distances from the disturbance, in contrast to the two-dimensional hydrostatic case. As a result, wave breaking in three dimensions often requires larger-amplitude topography since wave energy aloft can be dispersed laterally (Smith 2003). Furthermore, with access to the third dimension the flow can be deflected at low levels to pass around the obstacle rather than over it—a phenomenon known as flow splitting (e.g., Smith 1989b; Baines and Smith 1993). Flow splitting and lateral deflections reduce wave amplitudes and can significantly affect wave breaking in three dimensions, particularly for high obstacles (Epifanio and Durran 2001; Olafsson and Bougeault 1996). This study examines wave breaking

Corresponding author address: Nancy Soontiens, Department of Applied Mathematics, University of Waterloo, 200 University Ave. West, Waterloo, ON N2L 3G1, Canada.
E-mail: nksoonti@uwaterloo.ca

and lateral deflections in the context of flow over crater topography.

In addition to wave breaking, another interesting and important aspect of mountain waves is the development of severe downslope windstorms and hydraulic jumps for certain topographic and atmospheric profiles. The downslope windstorm is characterized by an intensification of lee-slope winds and topographic drag across the obstacle. It is often associated with wave breaking aloft. Several theories explaining its formation have been developed (e.g., Peltier and Clark 1979; Smith 1985; Durran 1986). Often associated with the downslope windstorm is a steepening of near-surface potential temperature contours and the formation of a structure that has been termed a hydraulic jump (e.g., Smith 2003; Armi and Mayr 2011). In this context, the hydraulic jump refers to a phenomenon where fast-moving fluid abruptly meets slower-moving fluid, causing steepening of streamlines. In addition, there is often a change in density (or potential temperature in the atmosphere) across the face of the hydraulic jump. The hydraulic jump is a key feature in the results presented in this article.

There is a growing interest in modeling atmospheric flows on planets other than Earth (e.g., Richardson et al. 2007). In the past, Martian lee waves have been analyzed mathematically by Pirraglia (1976) by considering a two-layer atmosphere and crater topography with a 100-km diameter. His analysis provided insights into the atmospheric wind profiles by comparing his results to observations for several sets of parameter values. Pickersgill and Hunt (1979) extended this work to include continuous stability and wind profiles and noted a ship-wake pattern of waves in the lee of the crater. Flow over craters on Mars may be of importance with respect to dust lifting and deposition, as indicated by observations of wind streaks in the lee of craters (Veverka et al. 1981; Lee 1984) and wind-tunnel experiments (Greeley et al. 1974a,b; Iversen and Greeley 1984). On Earth, large crater topography is less common, but a small crater with diameter 1 km was investigated by Fritts et al. (2010). Studies of flow over crater topography serve as an interesting extension to the common terrestrial-mountain-wave problem and can provide further understanding into topographic flows on Earth and on other planets. In addition, lee waves generated by craters of a large scale may be affected by the inclusion of rotation, which is examined in this study. Rotating flow over crater topography has been considered previously in the context of laboratory experiments by Davies et al. (1975).

This article examines mountain-wave features such as wave overturning and lateral deflections in the context of flow over crater topography using numerical simulations. Crater topography yields an interesting perspective

for orographic flows since both the shape and orientation of craters are fundamentally different from classical mountain wave studies. Craters are inherently three dimensional, so in contrast to the historical development of mountain-wave literature, craters should be considered in a three-dimensional perspective from the beginning. Classical predictions, such as wave-breaking height and the onset of flow splitting and upstream blocking, may not be valid for this topography shape. In addition, craters include several interesting topographic features such as elevated topography at the crater rims and depression topography through the crater depths. The features are reminiscent of other complex topographies, such as double hills, which often display wave interference between the two peaks and nonhydrostatic effects when the peaks are close together (Vosper 1996; Lee et al. 2006; Grubišić and Stiperski 2009). The vast literature on mountain waves provides a solid foundation for considering complicated orographic profiles such as craters.

An overview of the numerical methods and description of the simulations is provided in section 2. Section 3 outlines the results, with comparisons between two- and three-dimensional simulations, several atmospheric and topographic variations, and effects of rotation. The final section includes a summary and discussion of the results.

2. Methodology

Numerical simulations are performed using the Advanced Research dynamical core of the Weather Research and Forecasting (WRF) model in its idealized configuration (Skamarock et al. 2008). This model is used to integrate the fully compressible, nonhydrostatic equations of motion for an idealized atmosphere using a terrain-following vertical coordinate. In the simulations presented, the computational domain is 400 km \times 400 km horizontally and the domain top extends approximately to 30 km. The numerical grid has a horizontal resolution of $\Delta x = \Delta y = 500$ m and 200 grid points in the vertical. The grid is stretched vertically, which results in a resolution of $\Delta z \approx 120$ m near the surface and $\Delta z \approx 500$ m in the upper atmosphere. The vertical spacing does not exceed $\Delta z \approx 150$ m below $z = 15$ km. The lowest grid level is approximately 60 m above the surface. Most simulations are integrated to $t = 5$ h with time step $\Delta t = 5$ s, and a few are continued to $t = 10$ h for further investigation. No explicit horizontal or vertical mixing scheme is employed because the implicit sixth-order filter of the fifth-order upwind-biased advection scheme in the numerical model is sufficient (Wicker and Skamarock 2002). Simulations were performed on the General Purpose Cluster (GPC) supercomputer

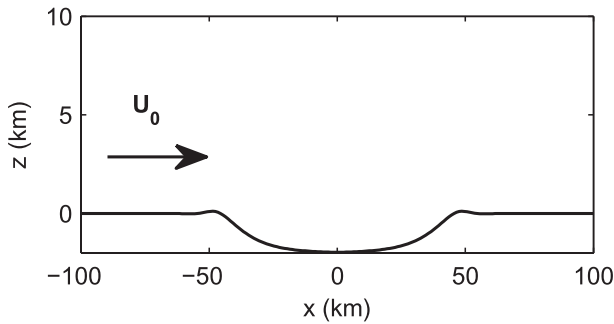


FIG. 1. The crater topography through $y = 0$. The crater has a diameter of 100 km and depth of 2 km. The rims are about 100 m high and 10 km wide. The direction of the background wind is indicated by the arrow.

at the SciNet High-Performance Computing (HPC) Consortium (Loken et al. 2010).

The topography is a circular crater centered at the origin with a diameter of 100 km and a depth of 2 km. At the crater edges, the surface is elevated slightly to represent the rimlike structure observed in many impact craters (Jankowski and Squyres 1992). A visualization of the crater topography through $y = 0$ is presented in Fig. 1. Several variations on the topography are also considered, such as a topography without rims and a crater with reduced diameter. Comparisons are also made with other studies, including the 1-km-diameter crater of Fritts et al. (2010) and the crater topography used by Pirraglia (1976) and Pickersgill and Hunt (1979), which only considers the crater rims and neglects the depression topography of the crater bowl.

The equations used to define the crater topography are given by

$$h(x, y) = \frac{h_0}{2} \left[1 - (1 + h_r) \operatorname{sech} \left(\frac{r - r_c}{2x_a} \right) \right] \times \left[-1 + \tanh \left(\frac{r - r_c}{x_a} \right) \right], \quad (1)$$

where

$$r = \sqrt{x^2 + y^2}.$$

The parameters h_0 , r_c , h_r , and x_a control the crater depth, crater radius, rim height, and crater wall slope, respectively. In the base case, these parameters are set to $h_0 = 2$ km, $r_c = 50$ km, $h_r = 0.1$, and $x_a = 5$ km. The result is the crater shape depicted in Fig. 1. The smaller crater is created by setting $r_c = 20$ km and $x_a = 2$ km. The crater without rims is created by requiring $h(x, y) \leq 0$. The crater dimensions were chosen to be in line with previous work on flow over crater topography (Pirraglia

1976; Pickersgill and Hunt 1979) and to approximately match with survey data of Martian crater profiles (Burt et al. 1976; Jankowski and Squyres 1992).

The atmosphere has a background wind speed $U_0 = 10 \text{ m s}^{-1}$ with open boundary conditions in the streamwise direction x and symmetric boundary conditions in the spanwise direction y . At the lower boundary, free-slip boundary conditions are used in line with other idealized studies of inviscid flow over topography (e.g., Bell and Thompson 1980; Lee et al. 2006). A Rayleigh damping layer begins at $z = 15$ km and extends upward in order to damp vertically traveling waves and prevent reflection from the upper boundary. The initial horizontal wind profile is

$$(u_0, v_0) = (U_0, 0).$$

The initial vertical velocity w_0 is zero except near the boundary where it is set by the WRF preprocessing system to prevent flow through the lower boundary (Skamarock et al. 2008).

Stratified flow over topography is characterized by several nondimensional numbers (e.g., Afanasyev and Peltier 1998). The Froude number,

$$F_r = \frac{U_0}{Nh},$$

compares the vertical scale of the topography h to the vertical scale of the gravity waves U_0/N , and characterizes the nonlinearity of the flow. Here, N is the buoyancy frequency, which is given by

$$N^2 = \frac{g \bar{\theta}'}{\bar{\theta} dz},$$

where g is the acceleration due to gravity and $\bar{\theta}$ is the background potential temperature profile. In the context of mountain waves, F_r governs nonlinear effects such as wave breaking and upstream blocking, which are favored when F_r is small. Since the generation of topographically forced waves is the main point of interest in this study F_r will be used to characterize flow conditions, although its applicability to waves generated by depression topography is less obvious than the typical mountain wave scenario. The crater depth is chosen as the vertical scale of the topography and $h = 2$ km is used in all definitions of F_r , which yields $F_r = 0.5$. It should be noted that in this framework F_r does not characterize upstream blocking, as it does in other mountain-wave problems. However, in the context of valley topography F_r has been used to classify sweeping and stagnant flows. In several numerical simulations and laboratory experiments,

TABLE 1. Summary of simulation parameters.

Description	N (s^{-1})	a (km)	F_r	F_a	R_o
Base case	0.01	100	0.5	0.01	—
2D base case	0.01	100	0.5	0.01	—
Reduced stratification	0.005	100	1	0.01	—
Two layer	0.01, $z > 0$	100	0.5, $z > 0$	0.01	—
No rims	0.01	100	0.5	0.01	—
Increased curvature	0.01	40	0.5	0.025	—
Rotation, base case	0.01	100	0.5	0.01	1
Rotation, two layer	0.01, $z > 0$	100	0.5, $z > 0$	0.01	1

Bell and Thompson (1980) found that a thermal stratification may be swept out of a valley when $F_r > 1.3$.

A second Froude number, which characterizes the nonhydrostatic effects, is given by

$$F_a = \frac{U_0}{Na},$$

where a is the horizontal scale of the topography. The diameter of the crater, $a = 100$ km, would seem to indicate that the flow is mainly hydrostatic with $F_a = 0.01$. However, we shall see that the simulation results display nonhydrostatic processes, such as the formation of a hydraulic jump–like feature. The nonhydrostatic effects are some of the most interesting aspects of this flow. This suggests that a needs to be chosen more appropriately, and this is discussed further below.

The importance of rotation is measured by the Rossby number

$$R_o = \frac{U_0}{fa},$$

where f is the Coriolis parameter. In the simulations with rotation we use $f = 10^{-4} s^{-1}$, which is typical of midlatitudes on Earth and Mars (Read and Lewis 2004). Taking a to be the diameter of the crater, $a = 100$ km gives $R_o = 1$, indicating that at this scale effects of rotation should be considered. In that light, simulations with and without rotation are performed for comparison.

A number of simulations with modifications to the atmospheric stratification and topography shape are considered in section 3. The base case with $F_r = 0.5$ and crater topography depicted in Fig. 1 is examined first. Next, a two-dimensional version using a cross section of the topography through $y = 0$ is analyzed. Other variations on the base case are also considered, including a reduced stratification and an atmosphere with an unstratified layer inside the crater, henceforth referred to as a two-layer stratification. The topographic modifications include a crater without rims and a crater with reduced diameter. Finally, effects of rotation are applied

to the base case and to the atmosphere with the two-layer stratification. The important parameters for each simulation are outlined in Table 1.

3. Results

a. Base case, $F_r = 0.5$

First, the base case with $N = 0.01 s^{-1}$, $U_0 = 10 m s^{-1}$, and $F_r = 0.5$ without rotation is examined. The main features of this flow are displayed in the vertical cross sections of the streamwise and vertical velocities through the crater center, $y = 0$ (Fig. 2). A primary beam of waves is visible over the leading crater edge in both cross sections. These waves have vertical wavelength $\lambda_z \approx 6$ km, which matches the wavelength expected in the hydrostatic limit, $\lambda_z = 2\pi U_0/N$. In addition, there is a set of waves of the same wavelength over the trailing crater edge. These waves are much weaker and have smaller amplitude, likely because of the near-stagnant fluid within the crater. The stagnant fluid effectively diminishes the topographic influence of the trailing crater slope through a reduction in the effective topographic height. In addition, the characteristic horizontal length scale has increased since much of the topography's shape and slope is masked by the stagnant fluid. The result is a weaker beam of waves over the trailing edge; however, the wavelength remains the same since N and U_0 are unchanged.

Another interesting feature is the interaction of the low-level jet along the leading crater slope with the relatively slow moving fluid within the crater bowl. The result is the formation of a hydraulic jump–like feature between $x \approx -38$ and -35 km from $t = 2$ to 4 h. This feature is clearly defined in the streamwise velocity and potential temperature contours from Fig. 2. The hydraulic jump has interesting implications for this type of flow. For one, the crater rim height is smaller than the height of the hydraulic jump, which is about 1 km at $t = 4$ h in Fig. 2g. In fact, the hydraulic jump height is comparable to the depth of the crater. As such, it could act as a modified topography, forcing additional gravity waves or causing lateral deflections or a combination of both. The Froude number based on the hydraulic jump height is $F_r = 1$. From the perspective of previous mountain wave studies, upstream effects become important at this value of F_r (e.g., Baines 1987). In addition, an alternative definition of F_a could be formulated using the distance from the crater rims to the hydraulic jump ($a \approx 15$ km) or the length of the jump head ($a \approx 5$ km). Respectively, these choices give $F_a = 0.067$ and $F_a = 0.2$, which are relatively large compared to the original choice of F_a using the crater diameter, indicating

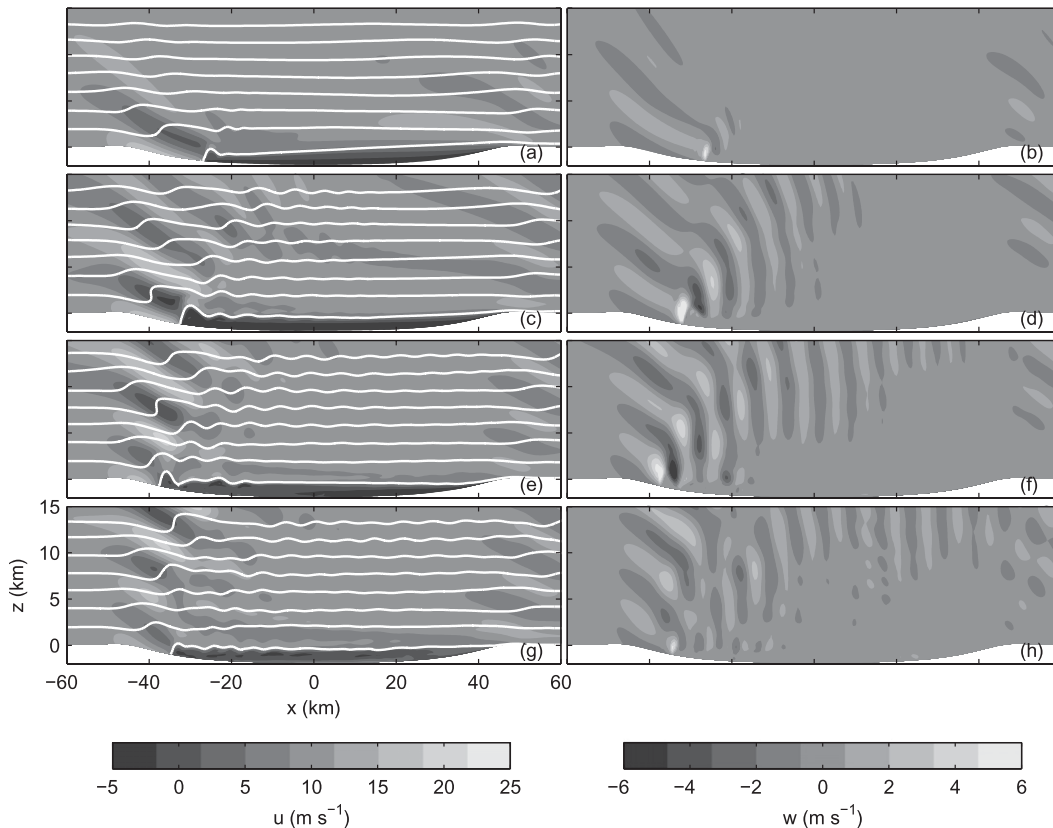


FIG. 2. Results from the three-dimensional $F_r = 0.5$ simulation. (a),(c),(e),(g) Streamwise velocity overlaid with white potential temperature contours through the crater center ($y = 0$) and (b),(d),(f),(h) vertical velocity. The potential temperature contours are $\theta = [288, 294, 300, 306, 312, 318, 324, 330]$ K. The output times are $t =$ (a),(b) 1, (c),(d) 2, (e),(f) 3, and (g),(h) 4 h.

that nonhydrostatic effects may be more important than what was first suggested. Examining the vertical velocity plots, there are indeed secondary gravity waves over the crater center that are believed to be generated by the hydraulic jump acting as a modified topography (Smith 2003). This explanation, along with other three-dimensional aspects of the hydraulic jump, is discussed further below.

Next, a close examination of the evolution and formation of the hydraulic jump is presented. As mentioned previously, the fluid within the crater depression is relatively stationary. However, at early times, this fluid is not entirely stagnant. In Fig. 2a, at $t = 1$ h, streamwise velocities within the crater depression reach a minimum of -10 m s^{-1} , indicating flow reversal. The low-level jet along the leading crater slope interacts with the cooler air within the crater, causing the steepening of potential temperature contours along the front and tilting of potential temperature contours toward the lee crater slope. At early times (see Fig. 2a at $t = 1$ h), the cooler air is pushed further into the crater, similar to a chinook front noted in other studies (Kerr 1986; Peltier

and Scinocca 1990; Afanasyev and Peltier 1998). Propagation of the chinook front is halted because of potential energy constraints since the cold crater air cannot be advected entirely out of the crater depression. The flow then reverses, forming a retreating gravity current. The gravity current is illustrated by the lowest potential temperature contours at times $t = 1$ and 2 h. This process is similar to the oscillations reported by Fritts et al. (2010) in numerical experiments of flow past a crater with a 1-km diameter (two orders of magnitude smaller than our crater). Their results show oscillations within the crater which they describe as a seiche behavior. Based on this hypothesis, they include several simulations with oscillatory forcing to examine the possibility for sloshing and cold air mixing under seiche conditions. According to the calculations used by Fritts et al. (2010), the seiche period for the craters presented here would be $T_0 \approx 2.7$ h. In our simulations, no significant seiche behavior persists for long times, perhaps because of the vastly different scales of the craters. After $t = 5$ h, the potential temperature contours remain relatively flat and the position of the hydraulic jump varies between

$x = -37$ and -33 km. More specifically, between $t = 4$ and 8 h the position of the hydraulic jump is almost stationary around $x = -34$ km, but varies slightly between $x = -35$ and -33 km. Between $t = 8$ and 10 h, the position of the hydraulic jump gradually moves to $x = -37$ km. Since the air within the crater remains relatively stationary, the descending low-level jet at the leading crater slope interacts with the nearly still fluid and causes the hydraulic-jump feature to persist, even after adjustment of the retreating gravity current.

The retreating gravity current and hydraulic jump are interesting features of this flow that induce some unique wave patterns. The hydraulic jump appears to act as a modified topography, forcing a secondary beam of gravity waves over the crater center, visualized in the vertical velocity plots. At $t = 1$ h (Fig. 2a), the beam of secondary waves originates from $x \approx -30$ km, which corresponds to the location of the gravity current head. At $t = 2$ h, the secondary beam is more developed, although it exhibits some complicated patterns since the source of forcing area is not stationary. At later times, in Figs. 2f,h, the secondary waves are still very clear and appear to originate from the gravity current head, which acts as a modified topography. In a previous study, the concept of modified topography has been considered by Lee et al. (1989) in the context of mountain topography and cold pools. In their results, the presence of a cold pool trapped against the leeside of the topography results in a wave structure that can be attributed to a modified topography. When the cold pool is not trapped against the topography it is flushed downstream. In the large crater results presented herein, the cooler air cannot be flushed out of the crater because of the topography shape and the stored potential energy. The result is a hydraulic jump-like feature that forces a secondary beam of waves.

Some of the three-dimensional aspects of this flow are examined in the low-level streamwise and spanwise velocity plots of Fig. 3. This figure displays velocity contours at the first grid level from the terrain-following vertical coordinate, which places the contours at about 60 m from the surface. At an early time, the retreating gravity current is well defined in the streamwise velocity (Fig. 3a). The low-level jet along the leading crater slope is clearly halted by the head of the retreating gravity current. The horizontal structure of the gravity current front resembles the shape of the leading edge of the crater topography. At a later time in Fig. 3c, the gravity current head has advanced closer to the leading crater rim, but it remains relatively stationary at this point.

Lateral deflections are apparent in the examination of the spanwise velocity plots in Figs. 3b,d. The primary feature is the convergence of air toward the crater center,

$y = 0$, along the leading crater slope. This is abruptly halted by the gravity current head where the spanwise velocities diverge away from the crater center. At the leading crater edge, the spanwise velocities are directed toward the crater center, even though the topography is elevated along the rims. Previous work on lateral deflections and flow splitting in three dimensions discusses the tendency for air to be deflected around elevated topography for certain regimes of F_r and the aspect ratio of the topography (Smith 1989a; Bauer et al. 2000; Epifanio and Durran 2001). In the case of crater topography, the effect of the crater rims is masked by the downward slope of the crater bowl. Since the crater topography has two vertical length scales, the crater rim height and the crater depth, we can choose an alternate definition of F_r based on the crater rim height ($h = 100$ m). This definition gives $F_r = 10$. This calculation indicates that the crater rims should have less effect on the dynamics than the crater depth, which produces $F_r = 0.5$. In fact, work by Smolarkiewicz and Rotunno (1989) found that lateral deflections are small for $F_r \gg 1$. Our simulations match this result since the crater rims, with $F_r = 10$, cause no noticeable lateral deflections. At a later time, the gravity current has retreated farther up the leading crater slope but there are still lateral deflections at the front. However, the spanwise motion here is much different than at earlier times. It is more disorganized and forms alternating bands of positive and negative spanwise velocity in an almost wavelike pattern. This pattern is associated with the wavelike instabilities that form behind the gravity current at later times.

COMPARISON WITH A TWO-DIMENSIONAL SIMULATION

We have performed an analogous two-dimensional simulation to isolate three-dimensional effects of this flow. The two-dimensional version of the crater topography is taken as a cross section through the crater center, $y = 0$ (other topographic profiles were considered—e.g., cross sections through different y —but are not shown here). The crater center is the most appropriate profile for comparison since, because of symmetry, the spanwise velocity is negligible along this cross section in the three-dimensional results. The two-dimensional simulations presented below have the same resolution as the three-dimensional case.

The two-dimensional simulation also displays primary beams of waves over the leading and trailing crater edges that are visible in the streamwise velocity plots and potential temperature contours of Fig. 4. These waves have $\lambda_z \approx 6$ km, matching the results from the three-dimensional simulations. Another similarity is the

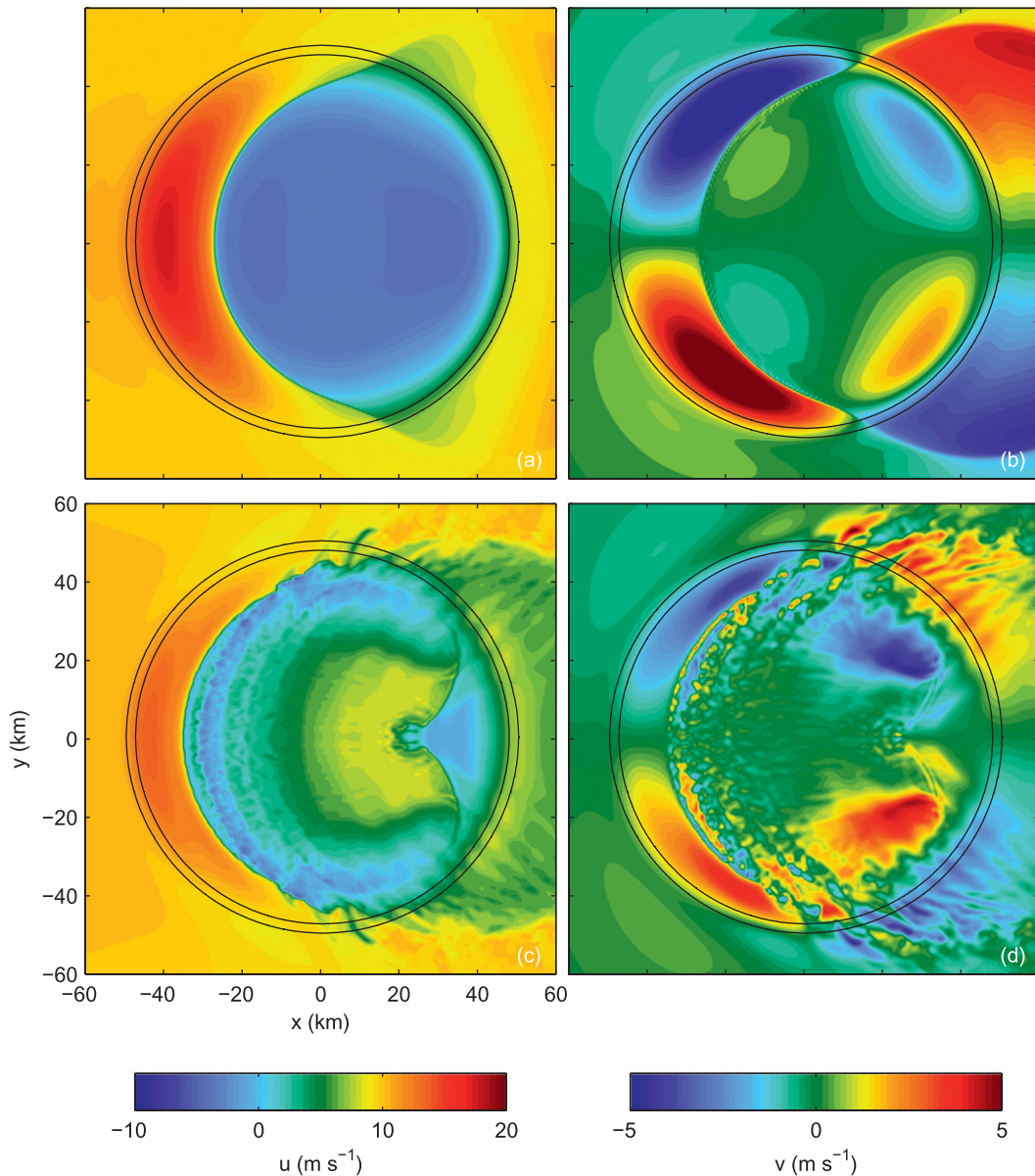


FIG. 3. Low-level velocities at the first grid level (terrain following, about 60 m above the surface). Shaded contours of (a),(c) streamwise velocity and (b),(d) spanwise velocity. The output times are $t =$ (a),(b) 1 and (c),(d) 4 h. The black circular contours indicate the crater rim peak.

position of the hydraulic jump at each time. The most noticeable difference between results in two and three dimensions is the overturning of potential temperature contours. This is first noticeable above the leading crater edge at $t = 2$ h and $z \approx 2$ km. At later times, overturning occurs higher in the atmosphere at heights $z \approx 7$ and 14 km. As outlined by Peltier and Clark (1979), in the case of the typical bell-shaped mountain in the hydrostatic limit the critical level for overturning z_c is related to the wavelength of vertically propagating waves by $z_c = (\frac{3}{4})\lambda_z$, which is 4.5 km here. Complex interactions

between the flow and retreating gravity current, as well as differences due to topography shape may result in lower levels of overturning for the crater topography. Note that measuring z_c from the crater bottom, $z = -2$ km, gives a prediction more in line with the results from Peltier and Clark (1979).

The degree of overturning is less intense in the three-dimensional simulation. In Figs. 2c,e, overturning, although less pronounced, occurs at the same heights as the two-dimensional simulations. However, it does not lead to the intense, small-scale motions observed in two

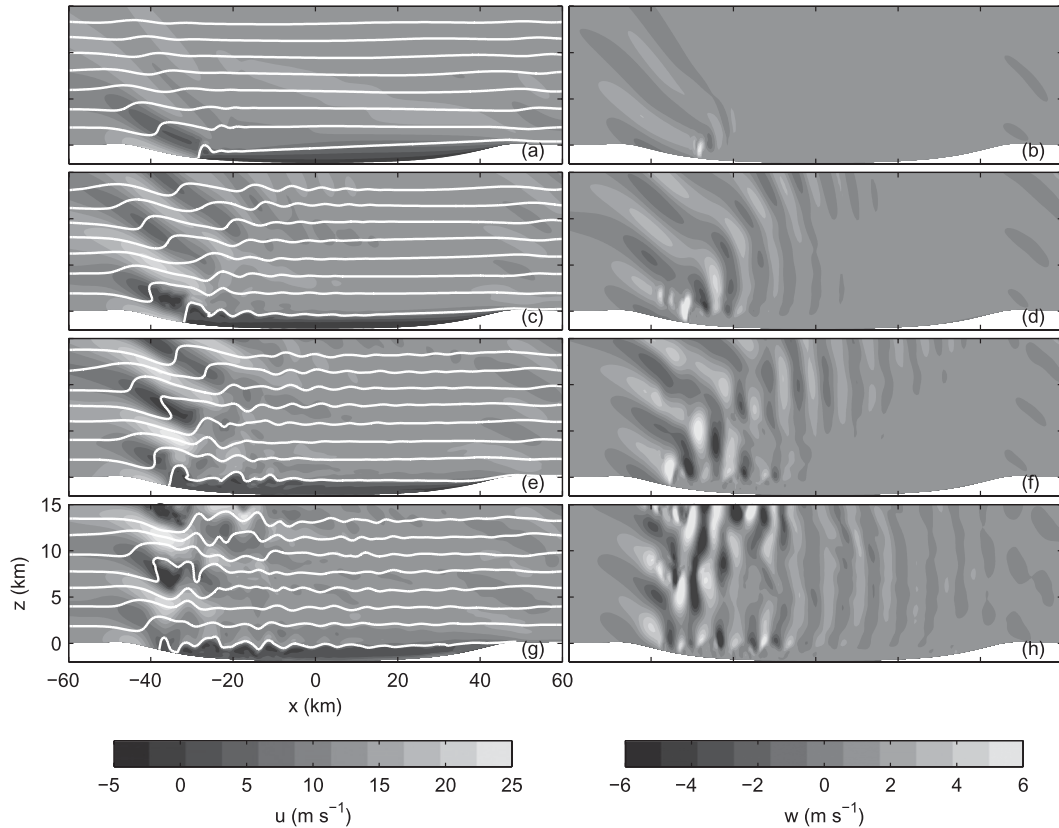


FIG. 4. As in Fig. 2, but for the two-dimensional $F_r = 0.5$ simulation.

dimensions. This difference is not caused by numerical damping since both simulations have the same resolution. It is clear that the wave-induced streamline steepness and vertical velocities are smaller in three dimensions. In addition, the wave amplitudes are up to 50% greater in the two-dimensional case. In other studies of wave breaking in two and three dimensions, the degree of overturning is generally overestimated in two-dimensional simulations owing to the complicated evolution of instabilities in three dimensions (Andreassen et al. 1994). Furthermore, in the three-dimensional ridge simulations by Epifanio and Durran (2001), low-level deflections around the topography effectively reduce vertical displacements and weaken upper-level wave amplitudes. With the crater topography, the crater rims do not cause outward deflections, but rather, the flow converges toward the crater center as it descends along the leading slope. Hence, low-level lateral deflections are not the cause of reduced overturning in three dimensions. Lateral dispersion of wave energy aloft could be responsible for the reduced wave amplitudes and overturning in three dimensions (Smith 2003).

In addition to increased episodes of overturning, the two-dimensional simulations include an upstream-propagating

disturbance most noticeable in Fig. 4g at $x \approx -38$ km near the surface. At later times, the upstream disturbance is very clear and decelerated flow extends upstream of the crater rims. In the three-dimensional case, no upstream-propagating disturbance is apparent beyond the times displayed in Fig. 2. Epifanio and Durran (2001) also observe a similar discrepancy between two- and three-dimensional flows. Their results indicate that in three dimensions the upstream disturbance disperses laterally and only extends a finite distance upstream of the topography, while in the two-dimensional case the disturbance propagates upstream indefinitely. In addition, Pierrehumbert and Wyman (1985) note an upstream-propagating disturbance, which they suggest is associated with wave breaking. This disturbance propagates arbitrarily far upstream in their infinitely long ridge simulations. In the crater simulations, the disturbance originates from the hydraulic jump, providing further evidence that it behaves as a modified topography. In addition, the disturbance is observed as far upstream as $x = -75$ km at $t = 8$ h, although it seems to have decayed in amplitude from earlier times (not shown here).

Overall, the main features of the two- and three-dimensional simulations are the same. The formation of

the primary beam of vertically propagating gravity waves, the hydraulic jump and retreating gravity current, and the secondary beam of waves forced by the gravity current are all present in both two and three dimensions. The main differences are the upstream-propagating disturbance and the degree of overturning, as discussed above. In a high-resolution, two-dimensional simulation with $\Delta x = \Delta y = 125$ m, these features are all present (not shown here), as well as resolved instabilities along the shear interface between the background flow and the stagnant fluid in the crater depths. These instabilities are also present in the lower-resolution two-dimensional simulation, manifested as wavelike patterns in Figs. 4f,h. With higher resolution, the instabilities are less organized and exhibit more small-scale features, but otherwise the results are the same. In three dimensions, it is unclear how these instabilities would evolve, and higher resolution would be necessary to capture their breakdown.

b. Atmospheric modifications

Several simulations with atmospheric modifications are considered in order to further examine the formation of the low-level jet and retreating gravity current. The simulations considered include a reduced stratification and a two-layer atmosphere.

1) REDUCED STRATIFICATION, $F_r = 1$

Since the stratification is a key factor in the development of the retreating gravity current and hydraulic jump, a simulation with lower buoyancy frequency has been examined. The interaction of cold air within the crater depression and warmer air entering the crater is ultimately responsible for the formation of the gravity current, hence reducing the stratification will impact the gravity current and the waves aloft. The buoyancy frequency has been reduced to $N = 0.005$ s⁻¹, which results in $F_r = 1$. This stratification is more typical of the Martian atmosphere, which has an average buoyancy frequency of $N = 0.006$ s⁻¹ (Read and Lewis 2004). Other studies focused on waves generated over crater topography in the Martian atmosphere (Pirraglia 1976; Pickersgill and Hunt 1979) concentrate on two-layer atmospheres with discontinuous velocity profiles. In both of these studies a ship-wake pattern of waves was produced in the lee of the crater.

The $F_r = 1$ simulation produces similar features to the base case. The streamwise velocity plots and potential temperature contours (Fig. 5) display the retreating gravity current and primary and secondary beams of waves. As warm air enters the crater valley, similar to a chinook front, it displaces the cooler air within, tilting the potential temperature contours. In this case, the chinook front propagates farther into the crater because of the reduced stratification. Once again, the cold air

cannot be pushed entirely out of the crater because of potential energy constraints and the flow reverses forming a retreating gravity current. The retreating gravity current is illustrated in Figs. 5e and 5g at times $t = 3$ and 4 h. The position of the gravity current head ranges between $x = -20$ and -8 km at later times. Examining the vertical velocity plots, it is clear that the retreating gravity current is responsible for forcing the secondary beams of waves within the crater.

Several important differences between this simulation and the base case should be noted. First, the wavelength of the primary beam of waves has been increased to $\lambda_z \approx 12$ km. This is expected and once again matches the vertical wavelength expected in the hydrostatic limit. Second, the chinook front propagates farther into the crater before it reverses as a gravity current. The reduced stratification lowers the amount of energy required to advect the cooler crater air. As a result, the hydraulic jump settles farther into the crater bowl than in the $F_r = 0.5$ case. Last, in an analogous two-dimensional version (not shown here), overturning levels occur higher in the atmosphere than in the base case, at $z \approx 2.5$ and 14 km.

2) TWO-LAYER ATMOSPHERE

Since the gravity current is an important feature of the flow, and appears to be ultimately responsible for the formation the hydraulic jump and secondary beam of waves, a two-layer atmosphere is considered in the next set of results. The two-layer atmosphere is constructed with constant potential temperature within the crater (i.e., below $z = 0$ km) and $N = 0.01$ s⁻¹ above. In this case, a gravity current should not be able to form and air passing into the crater should not be obstructed by a hydraulic jump.

The results are displayed in Fig. 6 by examination of the streamwise and vertical velocity plots and potential temperature contours. In this case, a low-level jet enters the crater and is not halted by the formation of a gravity current. Within the crater, overturning of the potential temperature contours occurs as the low-level jet progresses. In the base case, air passes over the gravity current, creating a shear layer between the stagnant fluid and background flow. In the two-layer atmosphere, the low-level jet proceeds underneath the stagnant fluid, causing overturning. The primary beam of waves is very similar in both cases, with matching wavelengths, although steepening of potential temperature contours at $z \approx 7$ km does not lead to overturning in the two-layer atmosphere. However, with the absence of the hydraulic jump no beam of secondary waves is present over the crater interior. Some vertical motion exists over the crater but is not as organized as in the base case.

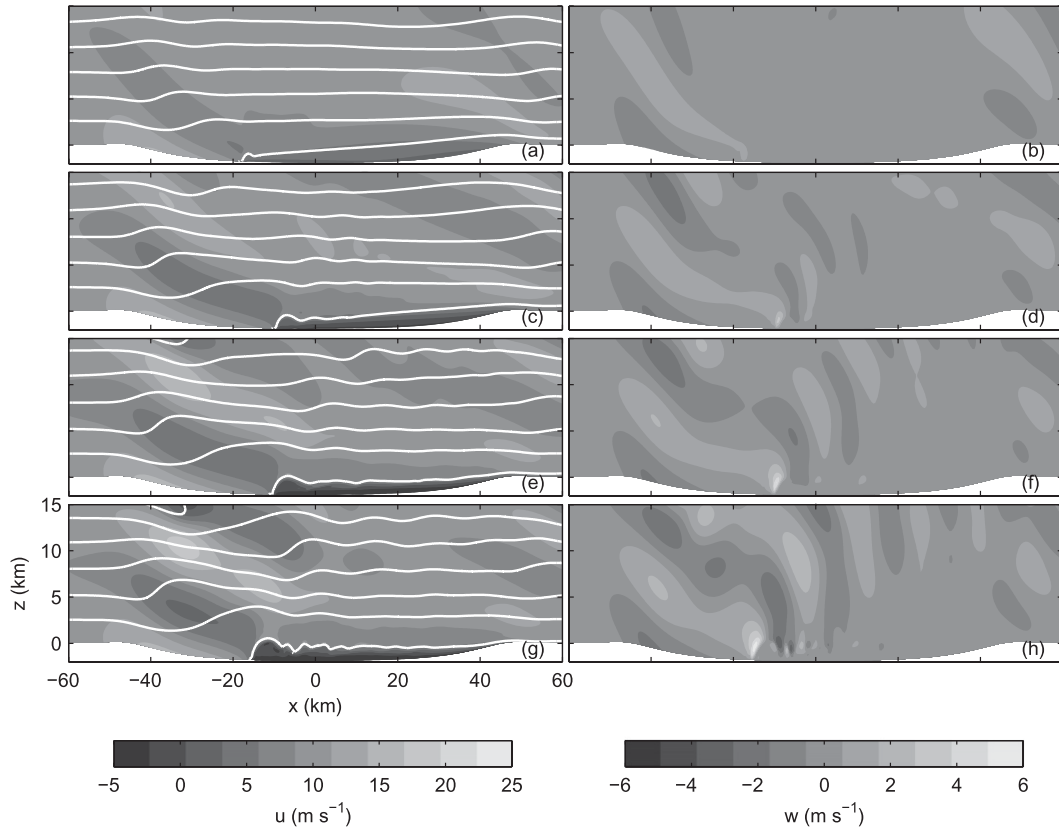


FIG. 5. As in Fig. 2, but for the $F_r = 1$ simulation. The potential temperature contours are $\theta = [288, 290, 292, 294, 296, 298, 300]$ K.

c. Topographic modifications

Several topographic modifications are considered in order to examine the wave patterns and retreating gravity current in the absence of crater rims and with an increased curvature. These cases will provide further insight into the three-dimensional aspects of the flow.

1) NO RIMS

The primary mechanism for wave forcing appears to be the descent of air into the depths of the crater, not flow over the rims. To further investigate the effect of the rims, we have included a simulation with the crater rims removed (Fig. 7). Once again, a primary beam of waves over the leading edge develops, along with a retreating gravity current and hydraulic jump within the crater. There is also some overturning in the lower part of the atmosphere, ahead of the hydraulic jump. The results in the front half of the domain are similar to the base case results, although the waves over the trailing edge are much weaker. It appears that the crater rims are influential for the development of waves over the trailing crater edge but have little impact on the waves over the leading crater edge and interior. At the trailing

edge, the near-stagnant fluid within the crater depths has effectively reduced the amplitude of the topography. Hence, the extra 100-m elevation from the crater rims is more important for exciting waves at the trailing crater edges, relative to the waves generated over leading edge.

2) CURVATURE

Further insight into the effect of topography shape on the flow evolution is obtained through an experiment with reduced crater diameter. The result is an increase in the topography's curvature, in addition to the slope of the crater walls. The crater curvature should have an effect on the spanwise deflection, similar to the impact that elongated ridges have on lateral deflections (Olafsson and Bougeault 1996; Epifanio and Durran 2001). In the next simulation, the diameter of the crater has been reduced to $a = 40$ km, giving $F_a = 0.025$. The Froude number governing nonlinear effects remains unchanged at $F_r = 0.5$. The domain size has been reduced to $200 \text{ km} \times 200 \text{ km} \times 30 \text{ km}$ since the crater diameter is much smaller. As a consequence, we were able to employ higher resolution so that the grid spacing

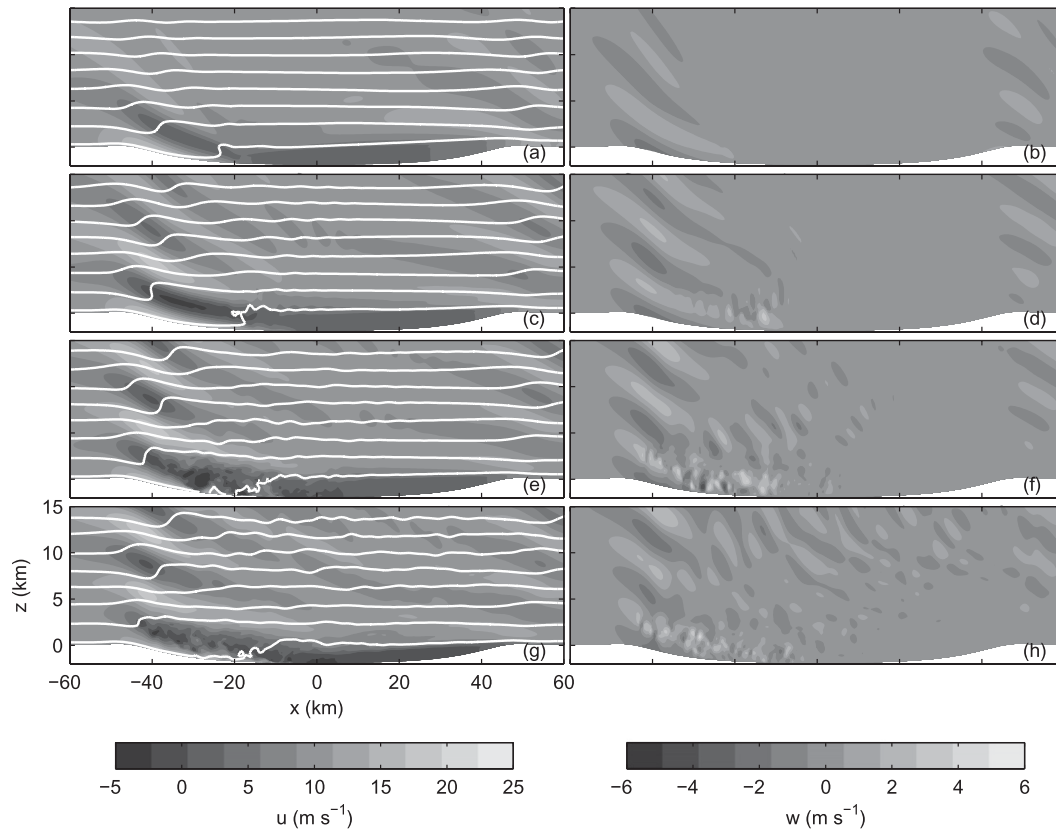


FIG. 6. As in Fig. 2, but for the two-layer atmosphere. The potential temperature contours are $\theta = [289, 295, 301, 307, 313, 319, 325, 331]$ K.

is $\Delta x = \Delta y = 250$ m in this simulation. The vertical resolution is unchanged.

Comparisons between the base case and the increased curvature case are presented in Figs. 8 and 9. The evolution of the flow through the crater center is visualized through vertical velocity plots in Fig. 8. Many features are similar to the base case simulations. Primarily, there are waves generated over the leading and trailing crater edges, in addition to secondary waves over the crater center. Compared to the base case, these waves make a larger angle with the vertical. At early times, the hydraulic jump-like feature is visible in the lowest potential temperature contour at $x \approx -15$ km, where it remains for later times. The hydraulic jump forms closer to the leading crater edge than in the base case, possibly because of the increased slope of the crater walls. Secondary waves are generated from this feature, most noticeably at the earliest time in Fig. 8b. At later times, these waves appear to interact with the primary waves since they are formed closer to the leading crater edge. In addition, instabilities are noted along the shear-layer interface between the stationary fluid within the crater and the fluid above. Upon careful inspection, these

instabilities appear in the three-dimensional base case as well, although with a much weaker intensity. They appear as wavelike structures along the shear interface, between $x = -10$ and -35 km in Figs. 2f and 2h. Ideally, higher resolution would be used to study these instabilities in three dimensions. In a high-resolution, two-dimensional simulation of the base case, the shear layer is active with small instabilities and overturning of potential temperature contours.

Finally, there is no overturning of potential temperature contours in this simulation. In the base case, a small degree of overturning was noted near the hydraulic jump. Because of the increase in curvature, it is expected that the smaller crater will induce more spanwise deflections. Hence, wave energy is more likely to be dispersed laterally, rather than into overturning. Notice in Figs. 8a,c that the wave amplitudes are comparable to the amplitudes in the base case. However, at later times, in Figs. 8e,g, the amplitudes near the surface have decreased. This is caused by the position of the hydraulic jump, which is much closer to the leading crater edge than at early times. The vertical topographic scale has effectively been decreased because of blocking by the

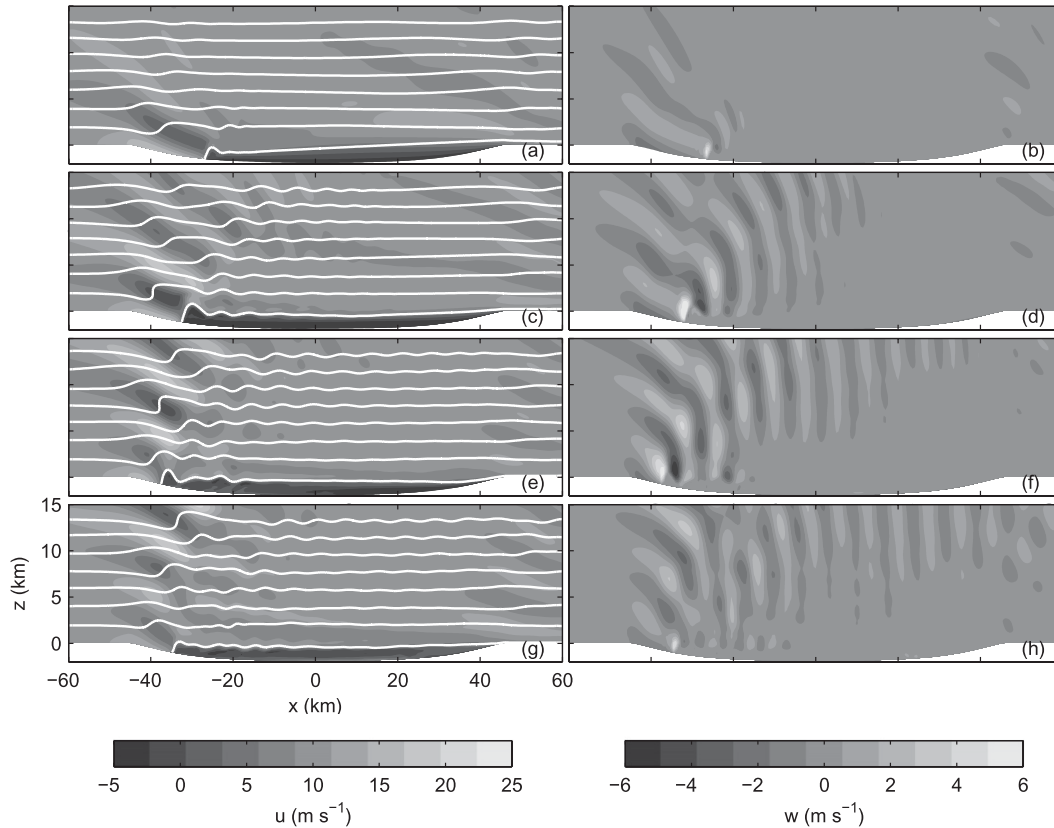


FIG. 7. As in Fig. 2, but for the simulation with no crater rims.

hydraulic jump; hence, we observe lower wave amplitudes. Perhaps this, in combination with lateral dispersion, is responsible for the lack of overturning in the smaller crater.

The structure of the spanwise velocity differs slightly between the base case and the crater with increased curvature (Fig. 9). At low levels both craters exhibit the convergence of air toward the crater center along the leading crater slope. The position of the hydraulic jump is apparent, indicated by an abrupt deflection toward the outer crater edges. At higher levels, the wave pattern is similar for both cases with outward stretching bands of positive and negative spanwise velocity in a wedgelike pattern. In addition, both cases exhibit vortical structures in the lee of the crater. The main difference is the location of maximum spanwise velocities. In the base case, the maximum spanwise velocities occur along the crater edges within the front half of the crater (near $x = -20$ km). The small crater shows maxima in the right half of the crater near $x = 15$ km. In addition, the smaller crater exhibits a more active spanwise velocity field in the right half of the crater (for $x > 0$ km), whereas the base case is almost devoid of spanwise motion in this region.

d. Rotation

Two additional simulations, including the effect of rotation, have been analyzed. These are the constant stratification with $N = 0.01 \text{ s}^{-1}$ and the two-layer atmosphere. The background wind is constant with $U_0 = 10 \text{ m s}^{-1}$ and the Coriolis parameter is set to $f = 10^{-4} \text{ s}^{-1}$, which is representative of midlatitudes. With the crater diameter 100 km, $R_o = 1$. This suggests that rotation may be important for these parameter values.

Results from these simulations are compared to the nonrotating cases in Fig. 10. Displayed are contours of the perturbation kinetic energy per unit mass, defined by

$$KE = (1/2)(u^2 + v^2 + w^2) - (1/2)(u_0^2 + v_0^2 + w_0^2), \quad (2)$$

where u , v , and w are the streamwise, spanwise, and vertical velocities, respectively. The contours are taken at the first grid level, about 60 m above the surface, from time $t = 4$ h.

The base case without rotation is shown in Fig. 10a and can be compared to the corresponding case with rotation in Fig. 10c. Both cases display similar features: a low-level jet along the leading crater slope, slow-moving

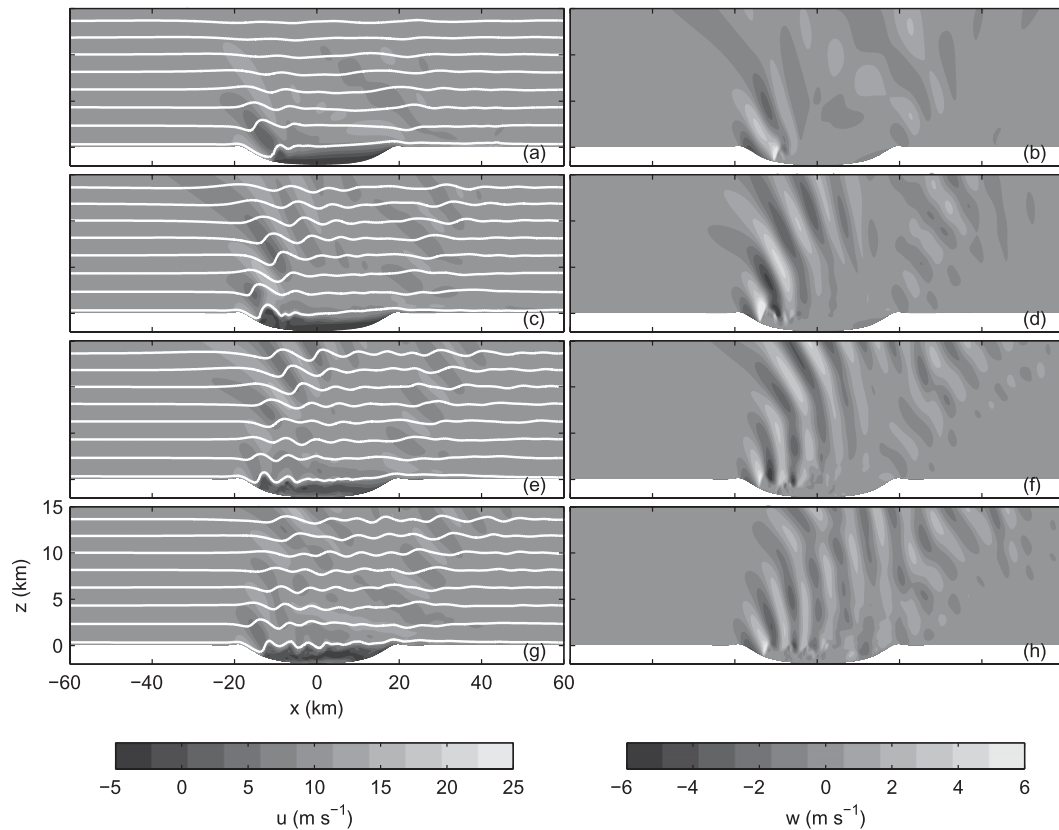


FIG. 8. Results from the modified crater simulations. As in Fig. 2, but at $t =$ (a),(b), 0.5, (c),(d) 1, (e),(f) 1.5, and (g),(h) 2 h.

fluid in the crater interior, and instances of breaking near the northern and southern crater edges ($y = \pm 50$ km). However, the symmetry is broken in the rotation case, which exhibits more breaking in the southern part of the crater. The results for the two-layer atmospheres are similar in Figs. 10b,d. The effect of rotation is to focus the breaking in the southern half of the domain. While there is still breaking above $y = 0$, there is more toward the southern crater edge. In the Northern Hemisphere, the rotation of the earth causes motion to be deflected to the right—hence, the increase of activity in the southern crater half. This is realized in the location of the maximum kinetic energy from the base cases with and without rotation. In the nonrotating cases, the maximum perturbation kinetic energy occurs along $y = 0$, whereas the maximum has shifted to the southern crater half in the rotating case. Hence, with high velocities focused in the southern half, one would expect increased episodes of overturning and small-scale motions.

Note that the effect of the gravity current is also clearly visible in these plots. The stratification within the crater and development of the retreating gravity current clearly block the flow from reaching the center of the

crater at low levels. Instead, the air is pushed up and over this feature. In contrast, the two-layer atmospheres exhibit large low-level velocities that extend far into the crater, which in turn induce more overturning and turbulence at low levels.

4. Discussion

The simulations presented in this study showcase the generation of internal waves over large crater topography in an idealized atmosphere. These simulations exhibit features similar to many other mountain wave and topographic flow studies, such as vertically propagating gravity waves, wave overturning, lateral deflections, and hydraulic jumps. A unique feature of these simulations is the formation of the hydraulic jump, which develops initially as a retreating gravity current when cold crater air cannot be advected out of the crater depression. The vertical scale of the hydraulic jump is comparable to the vertical topography scale, and as such the hydraulic jump acts as a modified topography forcing additional gravity waves. The plausibility of the gravity current explanation was examined through corresponding simulations in two dimensions and simulations with reduced

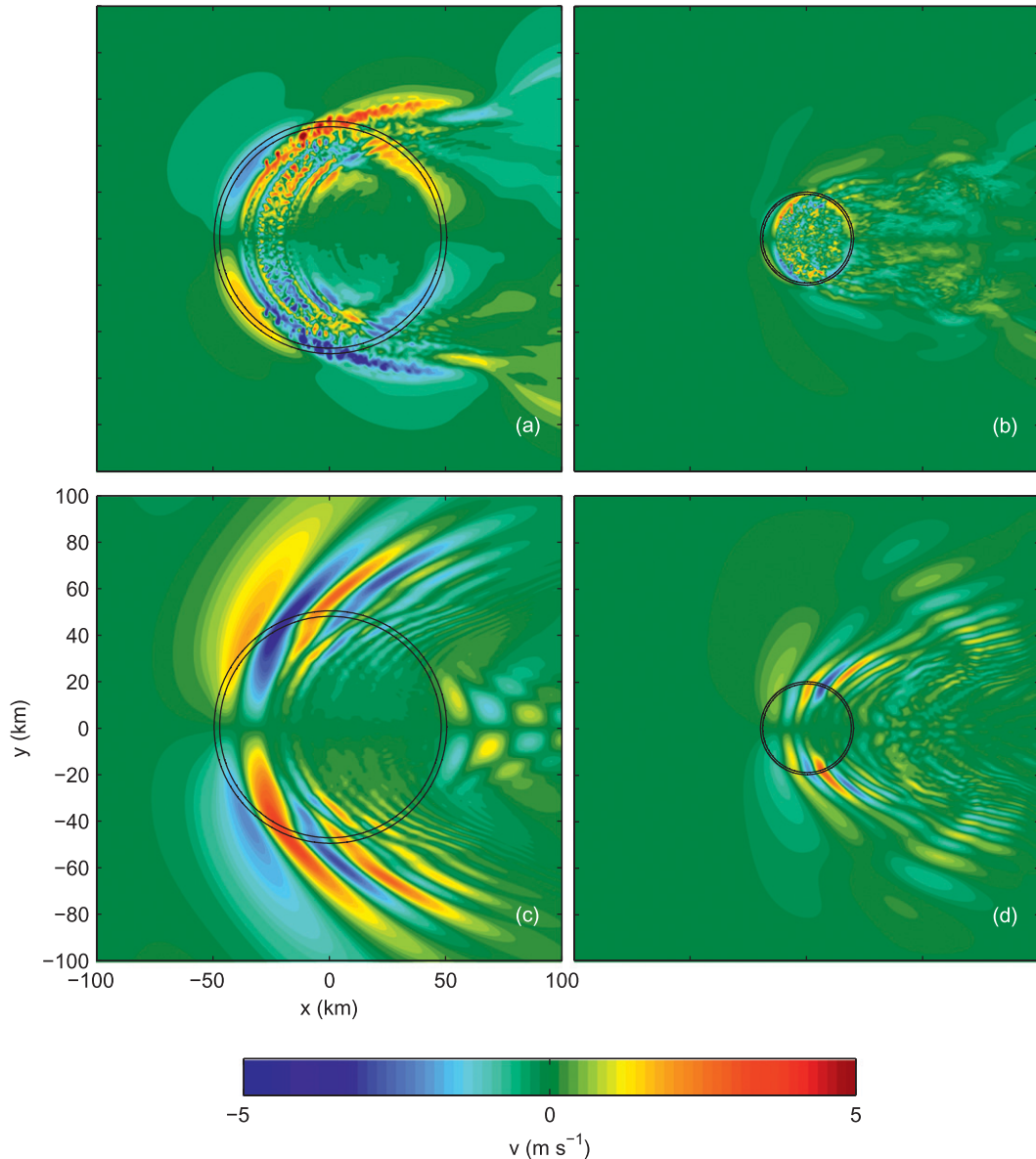


FIG. 9. Spanwise velocity from (a),(c) the base case and (b),(d) the simulation with smaller crater. The contours are from (a),(b) 1 and (c),(d) 10 km above the surface. The output time is $t = 3$ h.

stratification and constant potential temperature within the crater depression.

These results also provide insights into the differences of wave breaking and overturning in two and three dimensions. Generally, wave amplitudes in three dimensions are smaller than their two-dimensional analogs, requiring higher-amplitude topography for the onset of wave breaking in three dimensions. This discrepancy has, in part, been associated with lateral deflections, or flow splitting, as fluid passes around an obstacle rather than over it, effectively reducing vertical displacements and wave amplitudes. In the crater simulations, at

low levels there is a spanwise convergence of flow toward the crater center as it descends the leading crater slope. Hence, vertical displacements are not reduced because of low-level lateral deflections. Alternate explanations include lateral dispersion of wave energy aloft and the complicated evolution of wave instabilities in three dimensions. In addition, the elevated crater rims do not appear to cause any outward lateral deflections. In fact, a simulation with the crater rims removed indicates that the crater rims have little impact on the flow evolution except at the trailing edge. This work expands upon previous literature examining large

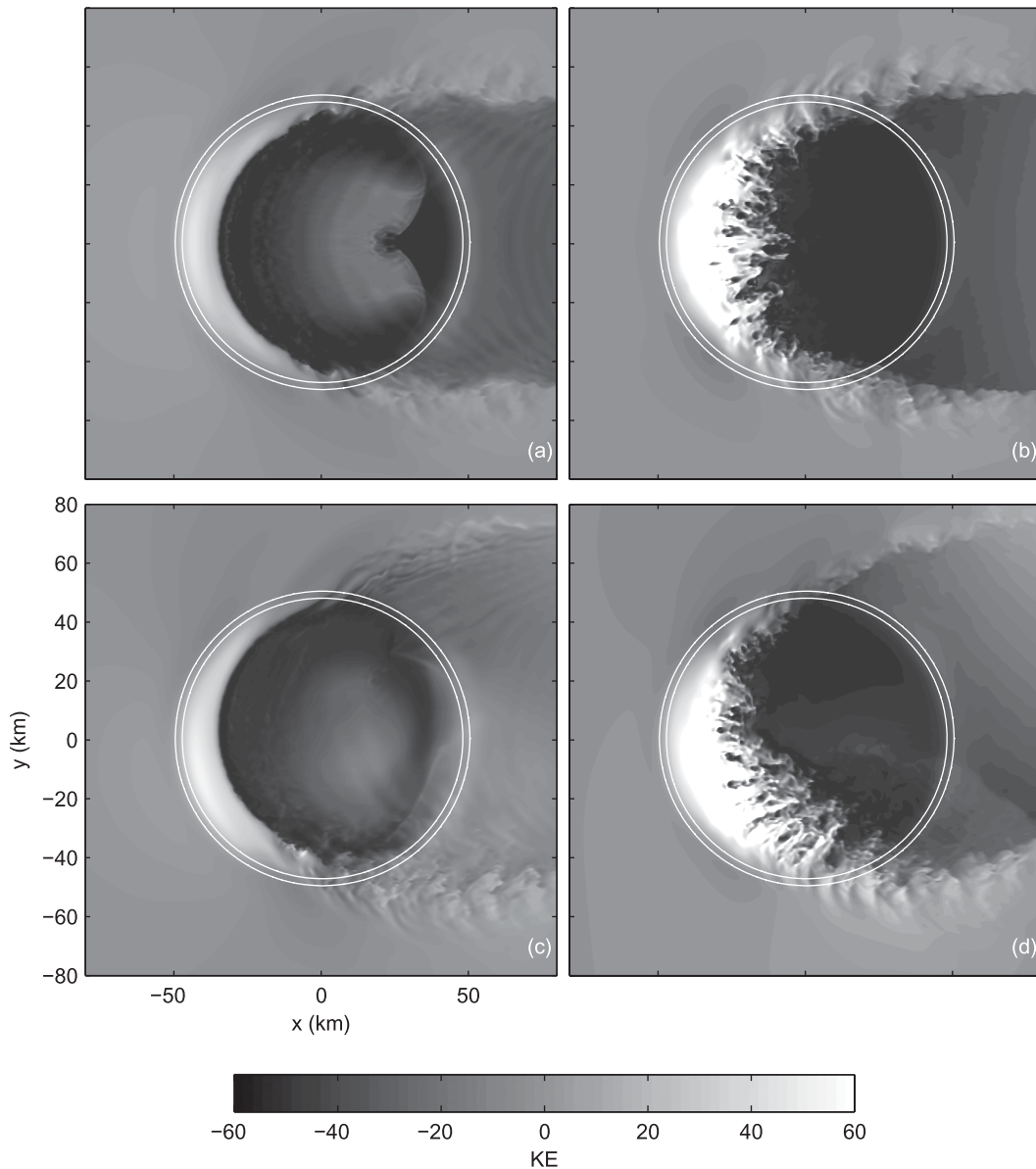


FIG. 10. Kinetic energy density at $t = 4$ h at the first grid level for several simulations: (a) base case, (b) two-layer atmosphere, (c) base case with rotation, and (d) two-layer atmosphere with rotation.

crater topography, which only considers the rims portion of the craters (Pirraglia 1976; Pickersgill and Hunt 1979).

In addition, these results examine flow over large crater topography, including the effects of rotation. Rotational flow over crater topography has been considered in a laboratory setting by Davies et al. (1975) but does not appear to have been considered in numerical simulations. The simulations with rotation indicate a preference for large low-level velocities in the southern crater half (below $y = 0$), which in turn induces more overturning in this part of the crater. The large velocities

are particularly noticeable in the two-layer atmosphere, where the low-level jet along the leading crater slope is not halted by the retreating gravity current. This result could have interesting implications for dust lifting in the Martian atmosphere. First, dust lifting around crater topography could be most expected in an atmosphere with a near constant potential temperature profile within the crater depression. This is supported by the observations of Veverka et al. (1981), who conclude that erosional streaks around crater topography are more likely after an event that reduces the atmospheric stability, such as the uniform heating of a dust storm. The

authors argue that atmospheric stability is more important than crater shape when considering dust erosion and deposition. In addition, the effects of rotation could provide a preference for dust lifting in one-half of the crater, depending on the hemisphere in which it is located. More comprehensive simulations with more accurate boundary layer dynamics, surface physics, flow separation, and dust-lifting parameterizations are required to examine this topic further.

Acknowledgments. This research was supported by the Natural Sciences and Engineering Research Council of Canada. Computations were performed on the GPC supercomputer at the SciNet HPC Consortium. SciNet is funded by the Canada Foundation for Innovation under the auspices of Compute Canada, the Government of Ontario, Ontario Research Fund—Research Excellence, and the University of Toronto.

REFERENCES

- Afanasyev, Y., and W. Peltier, 1998: The three-dimensionalization of stratified flow over two-dimensional topography. *J. Atmos. Sci.*, **55**, 19–39.
- Andreassen, Ø., C. E. Wasberg, D. C. Fritts, and J. R. Isler, 1994: Gravity wave breaking in two and three dimensions: 1. Model description and comparison of two-dimensional evolutions. *J. Geophys. Res.*, **99** (D4), 8095–8108.
- Armi, L., and G. Mayr, 2011: The descending stratified flow and internal hydraulic jump in the lee of the Sierras. *J. Appl. Meteor. Climatol.*, **50**, 1995–2011.
- Baines, P., 1987: Upstream blocking and airflow over mountains. *Annu. Rev. Fluid Mech.*, **19**, 75–95.
- , 1995: *Topographic Effects in Stratified Flows*. Cambridge University Press, 500 pp.
- , and R. Smith, 1993: Upstream stagnation points in stratified flow past obstacles. *Dyn. Atmos. Oceans*, **18**, 105–113.
- Bauer, M. H., G. J. Mayr, I. Vergeiner, and H. Pichler, 2000: Strongly nonlinear flow over and around a three-dimensional mountain as a function of the horizontal aspect ratio. *J. Atmos. Sci.*, **57**, 3971–3991.
- Bell, R., and R. Thompson, 1980: Valley ventilation by cross winds. *J. Fluid Mech.*, **96**, 757–767.
- Burt, J., J. Veverka, and K. Cook, 1976: Depth-diameter relation for large Martian craters determined from Mariner 9 UVS altimetry. *Icarus*, **29**, 83–90.
- Caccia, J.-L., B. Benech, and V. Klaus, 1997: Space-time description of nonstationary trapped lee waves using ST radars, aircraft, and constant volume balloons during the PYREX experiment. *J. Atmos. Sci.*, **54**, 1821–1833.
- Davies, P., D. Acheson, and C. Titman, 1975: A note on the geostrophic flow past a crater in a rotating fluid. *Geophys. Fluid Dyn.*, **7**, 119–131.
- Durran, D., 1986: Another look at downslope windstorms. Part I: The development of analogs to supercritical flow in an infinitely deep, continuously stratified fluid. *J. Atmos. Sci.*, **43**, 2527–2543.
- Epifanio, C., and D. Durran, 2001: Three-dimensional effects in high-drag-state flows over long ridges. *J. Atmos. Sci.*, **58**, 1051–1065.
- Fritts, D., D. Goldstein, and T. Lund, 2010: High-resolution numerical studies of stable boundary layer flows in a closed basin: Evolution of steady and oscillatory flows in an axisymmetric Arizona Meteor Crater. *J. Geophys. Res.*, **115**, D18109, doi:10.1029/2009JD013359.
- Greeley, R., J. Iversen, J. Pollack, N. Udovich, and B. White, 1974a: Wind tunnel simulations of light and dark streaks on Mars. *Science*, **183**, 847–849.
- , —, —, —, and —, 1974b: Wind tunnel studies of Martian aeolian processes. *Proc. Roy. Soc. London*, **A341**, 331–360.
- Grubisic, V., and I. Stiperski, 2009: Lee-wave resonances over double bell-shaped obstacles. *J. Atmos. Sci.*, **66**, 1205–1228.
- Gyüre, B., and I. János, 2003: Stratified flow over asymmetric and double bell-shaped obstacles. *Dyn. Atmos. Oceans*, **37**, 155–170.
- Holmboe, J., and H. Klieforth, 1957: Investigation of mountain lee waves and the air flow over the Sierra Nevada. Department of Meteorology, University of California, Los Angeles Final Rep. 133606, 290 pp.
- Iversen, J. D., and R. Greeley, 1984: Martian crater dark streak lengths—Explanation from wind tunnel experiments. *Icarus*, **58**, 358–362.
- Jankowski, D., and S. Squyres, 1992: The topography of impact craters in “softened” terrain on Mars. *Icarus*, **100**, 26–39.
- Kerr, R., 1986: Chinook winds resemble water flowing over a rock. *Science*, **231**, 1244–1245.
- Klemp, J. B., and D. K. Lilly, 1978: Numerical simulation of hydrostatic mountain waves. *J. Atmos. Sci.*, **35**, 78–107.
- Lee, S., 1984: Mars: Wind streak production as related to obstacle type and size. *Icarus*, **58**, 339–357.
- Lee, T., R. Pielke, R. Kessler, and J. Weaver, 1989: Influence of cold pools downstream of mountain barriers on downslope winds and flushing. *Mon. Wea. Rev.*, **117**, 2041–2058.
- Lee, Y., D. Muraki, and D. Alexander, 2006: A resonant instability of steady mountain waves. *J. Fluid Mech.*, **568**, 303–327.
- Loken, C., and Coauthors, 2010: SciNet: Lessons learned from building a power-efficient top-20 system and data centre. *J. Phys.: Conf. Ser.*, **256**, 012026, doi:10.1088/1742-6596/256/1/012026.
- Long, R., 1953: Some aspects of the flow of stratified fluids: I. A theoretical investigation. *Tellus*, **5**, 42–58.
- Olafsson, H., and P. Bougeault, 1996: Nonlinear flow past an elliptic mountain ridge. *J. Atmos. Sci.*, **53**, 2465–2489.
- Peltier, W., and T. Clark, 1979: The evolution and stability of finite-amplitude mountain waves. Part II: Surface wave drag and severe downslope windstorms. *J. Atmos. Sci.*, **36**, 1498–1529.
- , and J. Scinocca, 1990: The origin of severe downslope windstorm pulsations. *J. Atmos. Sci.*, **47**, 2853–2870.
- Pickersgill, A., and G. Hunt, 1979: The formation of Martian lee waves generated by a crater. *J. Geophys. Res.*, **84** (B14), 8317–8331.
- Pierrehumbert, R. T., and B. Wyman, 1985: Upstream effects of mesoscale mountains. *J. Atmos. Sci.*, **42**, 977–1003.
- Pirraglia, J., 1976: Martian atmospheric lee waves. *Icarus*, **27**, 517–530.
- Read, P. L., and S. R. Lewis, 2004: *The Martian Climate Revisited: Atmosphere and Environment of a Desert Planet*. Springer Verlag, 352 pp.
- Richardson, M., A. Toigo, and C. Newman, 2007: PlanetWRF: A general purpose, local to global numerical model for planetary atmospheric and climate dynamics. *J. Geophys. Res.*, **112**, E09001, doi:10.1029/2006JE002825.

- Skamarock, W., and Coauthors, 2008: A description of the advanced research WRF version 3. NCAR Tech. Note NCAR/TN-475+STR, 113 pp.
- Smith, R., 1980: Linear theory of stratified hydrostatic flow past an isolated mountain. *Tellus*, **32**, 348–364.
- , 1985: On severe downslope winds. *J. Atmos. Sci.*, **42**, 2597–2603.
- , 1989a: Hydrostatic airflow over mountains. *Adv. Geophys.*, **31**, 1–41.
- , 1989b: Mountain-induced stagnation points in hydrostatic flow. *Tellus*, **41**, 270–274.
- , 2003: Stratified flow over topography. *Environmental Stratified Flows*, R. Grimshaw, Ed., Kluwer Academic Publishers, 119–159.
- Smolarkiewicz, P. K., and R. Rotunno, 1989: Low Froude number flow past three-dimensional obstacles. Part I: Baroclinically generated lee vortices. *J. Atmos. Sci.*, **46**, 1154–1164.
- Veverka, J., P. Gierasch, and P. Thomas, 1981: Wind streaks on Mars: Meteorological control of occurrence and mode of formation. *Icarus*, **45**, 154–166.
- Vosper, S., 1996: Gravity-wave drag on two mountains. *Quart. J. Roy. Meteor. Soc.*, **122**, 993–999.
- Wicker, L., and W. Skamarock, 2002: Time-splitting methods for elastic models using forward time schemes. *Mon. Wea. Rev.*, **130**, 2088–2097.
- Wurtele, M., R. Sharman, and A. Datta, 1996: Atmospheric lee waves. *Annu. Rev. Fluid Mech.*, **28**, 429–476.